

**Resolving the location of small intracontinental earthquakes using
Open Access seismic and geodetic data: lessons from the 18
January 2017 m_b 4.3, Niger, earthquake**

Timothy J. Craig

COMET, School of Earth and Environment, The University of Leeds,
Leeds, United Kingdom. LS2 9JT

Corresponding author: t.j.craig@leeds.ac.uk

Steven J. Gibbons

NGI, Sognsveien 72, N-0855 Oslo, Norway

This submission is a non-peer reviewed preprint, available via EarthArXiv

Resolving the location of small intracontinental earthquakes using Open Access seismic and geodetic data: lessons from the 18 January 2017 m_b 4.3, Niger, earthquake

Timothy J. Craig

COMET, School of Earth and Environment, The University of Leeds,
Leeds, United Kingdom. LS2 9JT

t.j.craig@leeds.ac.uk

Steven J. Gibbons

NGI, Sognsveien 72, N-0855 Oslo, Norway

January 11, 2022

Abstract

A low-magnitude earthquake was recorded on January 18, 2017, in the Ténéré desert in Niger. This intraplate region is exceptionally sparsely covered with seismic stations and the closest open seismic station, G.TAM in Algeria at a distance of approximately 600 km, was unusually and unfortunately not operational at the time of the event. Body-wave magnitude estimates range from m_b 4.2 to m_b 4.6 and both seismic location and magnitude constraints are dominated by stations at teleseismic distances. The seismic constraints are strengthened considerably by array stations of the International Monitoring System for verifying compliance with the Comprehensive Nuclear Test-Ban-Treaty. This event, with magnitude relevant to low-yield nuclear tests, provides a valuable validation of the detection and location procedure for small land-based seismic disturbances at significant distances. For seismologists not in the CTBT system, the event is problematic as data from many of the key stations are not openly available. We examine the uncertainty in published routinely-determined epicenters by performing multiple Bayesloc location estimates with published arrival times considering both all published arrival times and those from open stations only. This location exercise confirms lateral

uncertainties in seismologically-derived location no smaller than 10 km. Coherence for InSAR in this region is exceptionally high, and allows us to confidently detect a displacement of the order 6 mm in the time-frame containing the earthquake, consistent with the seismic location estimates, and with a lateral length scale consistent with an earthquake of this size, allowing location constraint to within one rupture length (≤ 5 km) – significantly reducing the lateral uncertainty compared with relying on seismological data only. Combining Open Access-only seismological and geodetic data, we precisely constrain the source location, and conclude that this earthquake likely had a shallow source. We then discuss potential ways to continue the integration of geodetic data in the calibration of seismological earthquake location.

Keywords: Earthquake source observations, Seismicity and tectonics, Satellite geodesy, Earthquake hazards, Earthquake monitoring and test-ban treaty verification

1 Introduction

On the 18th January, 2017, a small-magnitude earthquake occurred in the Ténéré desert of northern Niger (Figure 1a). Located at the northern edge of the Sahel, bordering the Sahara, and roughly half way between the coasts of West Africa and the Red Sea, the source region is deep in the interior of Africa, far from any major population centres – the nearest city being Agadez, ~ 400 km away. The region is similarly remote from a tectonic perspective - the nearest active plate boundaries are in northern Morocco (~ 2000 km), the Gulf of Suez (~ 2400 km) and the East Africa Rift System (≥ 3000 km). The nearest instrumentally-recorded earthquake to the 2017 event, of any magnitude, in the combined catalogues of Bulletin of the International Seismological Centre (ISC Bulletin hereafter; ISC (2021)), is a similarly-remote $m_b 4.5$ earthquake in the southern Ahaggar mountains of Algeria, ~ 600 km away. Within 15 degrees (~ 1650 km) of the Ténéré earthquake, there are only 625 earthquakes reported in the full ISC Bulletin, of any magnitude.

As a result of the tectonic quiescence and remoteness of the region, Ténéré is one of the least-well seismologically instrumented continental regions on Earth, with the nearest seismic station located over 600 km away (at Tamanrasset, southern Algeria - which was in fact inoperative at the time of this earthquake), and no other stations within 1000 km. For small-magnitude earthquakes, data from seismic networks at local and regional distances is crucial for the robust and accurate determination of the earthquake location (e.g. Bondár et al, 2004). In the absence of such data, the 2017 Ténéré earthquake offers an opportunity to test the resolving power of global seismic networks, and the limitations of seismological location routines in the absence of near-field data. With the lack of vegetation, and the lack of major agricultural or industrial activity in the area, the Ténéré desert is also a region where the coherence of interferometric synthetic aperture

25 radar (InSAR) images is high, enabling the detection of small-magnitude surface displace-
26 ments, and we thus also aim to test how satellite geodesy can complement seismological
27 approaches in the location of small earthquakes in remote continental areas.

28 Routine seismological catalogues determined the location ($\sim 19.6^\circ N, 10.6^\circ E$), and
29 magnitude ($m_b 4.2 - 4.6$) of this earthquake (see Table 1). The reported magnitude
30 of this earthquake places it in the range of interest for low-yield nuclear tests. For such
31 events, routine seismological monitoring is supplemented by the observational capabilities
32 of the International Monitoring System (IMS), under the auspices of the Comprehensive
33 Test Ban Treaty Organisation (CTBTO), most particularly through a global network of
34 small-aperture seismic arrays and high-quality three-component seismometers. However,
35 data from many of these networks remain subject to access restrictions, and are not
36 currently freely available to the scientific community. This study probes how far events
37 like the Ténéré earthquake can be studied and characterised in detail using only freely-
38 available Open Access data, and tests how reliant the location of such earthquakes is on
39 closed-access data. We combine remote seismological and geodetic analysis to assess the
40 validity with which routine processing approaches were able to determine the location
41 of this earthquake. We highlight a number of issues that may cause problems for the
42 location of rare small earthquakes in remote continental interiors, and demonstrate how
43 the combination of careful seismological analysis with modern geodetic data can mitigate
44 such problems, allowing the high-resolution characterisation of such events.

45 2 Overview of the Seismological Observations

46 Figure 1 displays the source region of the January 18, 2017, earthquake together with
47 the locations of events in the ISC GEM catalog (ISC-GEM, 2021) (unrestricted) and
48 the ISC Bulletin (limited to those within 15°), and the locations of seismic stations
49 used to constrain the location in the bulletins listed in Table 1. The map in panel (a)
50 confirms both the absence of significant seismic events in an almost continental-scale
51 region surrounding the epicenter and the sparsity of stations at local, regional, or far-
52 regional distances contributing to the location estimates. Of those stations at far-regional
53 distances (a term usually referring to distances between 10° and 20°) only the three-
54 component station GT.DBIC in the Ivory Coast is open for public access. Panels (b),
55 (c) and (d) of Figure 1 show the signal on GT.DBIC both in a high frequency bandpass
56 (1-4 Hz) and the lower frequency band from 12.5 s to 50.0 s period. The short-period
57 band signals are typical of far-regional continental propagation with high frequency Pn
58 and Sn arrivals followed by high-amplitude and slightly lower period Lg waves which
59 dominate the wavetrain. Both Pn and Sn arrivals are followed by long codas with high-
60 frequency energy. Both body waves and surface waves are visible in the longer period
61 signal although the Pn and Sn arrivals have low Signal-to-Noise Ratio (SNR). Only

62 the Pn arrival is particularly useful for location purposes; the Sn arrival is extremely
63 emergent and picking an accurate signal onset is difficult. In addition, even if the Pn
64 arrival-time can be read accurately, the distance-range for this station is associated with
65 an exceptionally large uncertainty in the modelled traveltime (e.g. Myers et al, 2015). The
66 primary value of the DBIC signal is in the estimation of magnitude and the hypothesis
67 that the event is relatively shallow in order to explain the dominant Lg and surface waves.

68 Figure 2 provides both a representative selection of the available teleseismic waveforms
69 and an overview of the global station coverage, again differentiating between stations open
70 to the general public and those limited to authorized parties in the CTBT system. For
71 a seismic event with significant continental landmass in all directions within distances of
72 100 degrees (i.e. where you would anticipate observing P -waves) there is an exceptional
73 degree of asymmetry to the observing seismic network. We have examined significant
74 numbers of open waveforms at stations not included in the ISC bulletin, but where
75 data is openly available (see Figure 1a), and found in very few cases signals which both
76 offered a high SNR and a useful location, covering an azimuthal or distance gap relative
77 to the network displayed in Figure 2. The best signals are found on stations to the
78 North East; in Eastern Europe and Central Asia – a distribution that will be the result
79 of both the network coverage, and the orientation of the focal mechanism and resultant
80 radiation pattern (note that the focal mechanism for this earthquake is unknown). Figure
81 2 shows signals on the vertical components of three 3-component stations, and (vertical
82 component) array beams on three array stations.

83 Of the waveforms shown on Figure 2, the Makanchi array (MKAR) is a 9-site primary
84 IMS seismic array in Kazakhstan, the Mount Meron array (MMAI) is a 16-site auxiliary
85 IMS seismic array in Israel, and the Bukovina array (BURAR) is a non-IMS 9-element
86 array in Romania. The data from all of these arrays are openly available; MKAR and
87 BURAR are available via the IRIS Data Management Center and MMAI is available via
88 the GEOFON data center at GFZ Potsdam. Each of these arrays has an aperture of
89 only a few km, with the intention that short period signals (e.g. 1-4 Hz) are coherent
90 between sensors and that the SNR of signal arrivals can be improved by delay-and-
91 stack beamforming (e.g. Rost and Thomas, 2009). Similarly, estimating the coherence
92 or relative power of beams in different directions allows us to estimate the backazimuth
93 and apparent velocity of incoming wavefronts. This assists in algorithms to associate
94 detections and helps to build confidence that a given signal detection is indeed associated
95 with our event hypothesis, on the basis of directional coherence of arrivals.

96 For each array in Figure 2, the top panel shows the array beam constructed using
97 the predicted backazimuth and P -wave slowness, based on the ISC location. Beneath
98 each of the array beams is a scan of backazimuth as a function of time (for a fixed
99 apparent velocity based on the expected earthquake epicentre) and a scan of apparent
100 velocity as a function of time (for a fixed value of the backazimuth based on the expected

101 earthquake epicentre). These plots are a variant on the VESPA process (Davies et al,
102 1971) and allow us to confirm that each of the signals at the time of the predicted P -
103 arrival is associated with a coherent wave packet with a direction consistent with the
104 origin hypothesis. Gibbons et al (2016) performed such analysis on several array stations
105 for an earthquake of similar magnitude near the Northern tip of Novaya Zemlya in the
106 Russian Arctic and found double bursts of coherent energy with a delay of just over 3
107 seconds at stations at different azimuths from the epicenter. This observation supported
108 a hypothesis of teleseismic pP phases which helped to constrain the event depth. There
109 is no such unambiguous evidence of depth phases in the array analysis in Figure 2.
110 BURAR and MMAI show very little coherent energy in the coda following the initial
111 arrival; MKAR shows coherent energy with appropriate propagation parameters far into
112 the coda.

113 The remaining three panels of Figure 2 show signals for the P-arrivals at arbitrarily
114 chosen teleseismic 3-component stations (in Czechia, Saudi Arabia, and Kenya). We note
115 that the SNR for the signals at many of these stations is relatively poor, and that im-
116 provement through stack-and-delay is not possible for non-array stations. The waveforms
117 shown in Figure 2 also highlight the potential subjectivity in identifying the onset of a
118 particular phase arrival, with the majority of arrivals being emergent, especially in terms
119 of identifying a confirmed signal above the level of noise. We see no unmistakable depth
120 phases, which would offer a high-precision constraint on the event depth. A few stations
121 show multiple bursts of energy but there is insufficient evidence at any station to label
122 with confidence the later arrivals as depth phases.

123 Summarising the available seismological data, we are left with a comparatively sparse
124 set of phase observations, of variable, but often limited, precision. The advantages in
125 signal identification and arrival precision that arise from the enhanced processing of
126 small aperture arrays is clear. But only a few of the operators of these stations make
127 their waveform data Open Access (see Figure 2). Similarly, many of the more isolated
128 three-component stations, vital for filling gaps in azimuthal and epicentral coverage,
129 remain closed to the general public. Combined, these pose the question of how reliant
130 high-precision earthquake location is on closed-access data, and how well characterised
131 events such as the Ténéré earthquake can be, using only Open Access seismic data.

132 **3 Seismic Location Estimates for the 18 January** 133 **2017 Niger Earthquake**

134 Figure 3 shows the epicenters listed in Table 1 together with the published 95% confi-
135 dence ellipses. The epicenters reported by the NEIC/USGS (National Earthquake In-
136 formation Center/United States Geological Survey) and CTBTO/IDC (Comprehensive

137 Nuclear Test-Ban-Treaty Organization/International Data Center) lie comfortably within
138 the confidence ellipse reported by the other agency, and there is significant overlap be-
139 tween the two confidence ellipses. The epicenter reported by the International Seismolog-
140 ical Center (ISC, 2021) lies within both of these confidence ellipses but is itself associated
141 with a much smaller confidence ellipse which does include the CTBT epicenter estimate,
142 but not the NEIC epicenter estimate. A fourth location estimate is provided in the ISC
143 catalog summary: the ISC-EHB estimate (ISC-EHB, 2021). This epicenter lies to the
144 southeast and outside of all of the other 95% confidence ellipses. The ISC-EHB estimate
145 itself is associated with a far smaller confidence ellipse which overlaps little with the
146 other 95% confidence ellipses. All of the confidence ellipses share a similar azimuth of
147 the semi-major axis: all around 120° . This is easy to understand in terms of the station
148 distribution (c.f. Figure 2) since the density of contributing stations in directions from
149 North to East (i.e. in Europe and Central Asia) is substantially greater than in other
150 directions.

151 Comparing the different epicenters and corresponding confidence ellipses is difficult
152 since the different solutions use different combinations of arrival-time readings, station
153 distributions, weights, and location algorithms. Only the NEIC and CTBT catalogs
154 are truly independent. Although they have some stations in common, the readings are
155 made by different analysts and using different systems and location procedures. The ISC
156 catalog, and the ISC-EHB solution, exploit phase readings from different catalogs and
157 can frequently use two different arrival time estimates, reported by different agencies,
158 for the same phase arrival to constrain an event. TORD in southwestern Niger and
159 KEST in Tunisia are two of the stations in the ISC bulletin that are closest to the
160 earthquake epicenter. Both stations are primary seismic stations of the International
161 Monitoring System and, to the best of our knowledge, the data from neither are available
162 to users other than those with access authorized by National Data Centers in the CTBT
163 system. The USGS has access to this data via the United States National Data Center
164 and is authorized to use arrival-time estimates from these stations when forming their
165 earthquake bulletin.

166 The ISC bulletin provides two estimates for the P_n arrival time at TORD: 21:50:53.534
167 and 21:51:02.71, reported by the IDC and the NEIC respectively. Only the first of these
168 is a defining phase in the ISC catalog, with a time residual of -0.7 seconds. The second
169 is labelled a “Questionable onset” (with a time residual of 8.5 seconds) and does not
170 contribute to the solution. The ISC bulletin also provides two estimates for the P_n
171 arrival time at KEST: 21:52:07.30 and 21:52:06.98, again provided by the IDC and the
172 NEIC respectively. Both of these arrivals (with time-residuals of -0.7 seconds and -1.0
173 seconds respectively) are defining arrivals in the ISC solution. In the ISC-EHB bulletin,
174 all four of these arrival times are defining phases for the location estimates with time
175 residuals listed as -2.1 seconds (TORD P_n , IDC), 7.1 seconds (TORD P_n , NEIC), -1.4

176 seconds (KEST P_n , IDC), and -1.7 seconds (KEST P_n , NEIC). The time residual on the
177 TORD P_n arrival is large for both the ISC and ISC-EHB solutions. The size of the time
178 residual led it to be disregarded from the ISC solution. While it is a defining phase in
179 the ISC-EHB solution, it is not easy to estimate the effect it has on the solution without
180 a thorough examination of the weights and the provenance of the location algorithm.

181 The discrepancy between the ISC-EHB epicenter and the other epicenters is likely
182 a combination of many such differences. The waveforms displayed in Figures 1 and 2
183 make it clear how emergent and ambiguous some of the phase arrival time estimates
184 may be. Often the highest amplitude comes several seconds after what appears to be
185 the first signal onset and we may have to make judgements regarding what is a likely
186 first P -arrival and what is a possible depth phase. The first part of the signal visible
187 above the background noise may be significantly later than the true onset time if we have
188 an emergent signal or a depth phase with a higher amplitude than the first P -arrival.
189 Without access to the waveform data, it is not possible for an independent seismologist
190 to evaluate the quality of the arrival time estimates, limiting our ability to determine
191 where pick uncertainty may be driving the discrepancies in location estimates.

192 However, we can gain more understanding as to how the location estimates depend
193 upon the choice of stations alone by performing new location estimates using a common
194 algorithm with the arrival times used for the different catalogs displayed in Figure 3. We
195 use the Bayesloc program (Myers et al, 2007) which can solve for the locations of multiple
196 seismic events simultaneously by a Monte Carlo Markov Chain (MCMC) procedure to
197 find a joint probability distribution for the events' origins, origin parameter uncertainties,
198 and for empirical corrections to modelled traveltimes. Although the program is designed
199 for, and is most effective with, large clusters of seismicity, it can also be run for a single
200 event. For each iteration of the MCMC routine, the program writes out the epicenter
201 coordinates. Over a single run, many thousands of origin hypotheses are written out
202 generating a cloud. The size and shape of this cloud provides a visualization of the
203 uncertainty associated with the location which may show a more complex geometry than
204 the classical formal confidence ellipses.

205 Figure 4 displays the clouds of trial epicenter estimates from the Bayesloc calculations
206 for four different combinations of stations. In panel (a) the event is located using only the
207 phase arrival times listed in the USGS/NEIC bulletin. The red symbols are the epicenters
208 output when we only use those stations for which waveform data can be obtained without
209 barrier by an arbitrary user from only open sources (red symbols in panel (b)). The grey
210 symbols are the epicenters output when we also allow use of the arrival times from stations
211 for which waveform data are not available without specific authorization (white symbols
212 in panel (b)). We attempt to better visualize the spread of the point clouds by plotting
213 the 90, 95, and 99% confidence ellipses based upon the statistics of the coordinates,
214 although we stress that the point cloud distributions may display significant departures

215 from the geometries indicated by the ellipses. The inclusion of the closed access stations
216 reduces the apparent spread somewhat although the difference is not large. As noted
217 earlier, the TORD arrival in this dataset is associated with a large time-residual and so
218 it may have had very little influence on the solutions. We note also that the Bayesloc
219 epicenter clouds using the USGS/NEIC arrival estimates are consistent with the bulletin
220 epicenter estimate.

221 Panel (c) of Figure 4 shows the corresponding Bayesloc epicenter clouds for the ar-
222 rivals listed in the ISC bulletin, with the corresponding station maps displayed in panel
223 (d). There is a significant difference between the spread of the epicenter clouds for the
224 “complete” and “strictly open” station networks for the ISC arrivals. We note that not
225 only is the TORD time-residual far smaller for one of the arrivals in the ISC solution,
226 but there are 3 other network stations, KIC, TIC, and LIC which add extra constraints
227 from the South West. These stations are all very close to DBIC, in the Ivory Coast, and
228 they do not much increase the azimuthal coverage. However, their inclusion may change
229 the weight of the constraints from that direction considerably. We note in addition, an
230 extra constraint from the Soneca Array (ESDC) in Spain from the CTBT bulletin. This
231 is in a direction in which there are no open stations with good signals or clear picks. This
232 may be an example of where the use of beamforming of signals on a seismic array may
233 make a usable phase arrival where one was not sufficiently strong on a single channel,
234 allowing the identification of arrivals even in regions where the radiation pattern leads
235 to comparatively low amplitudes. The Bayesloc epicenter clouds lie a few km to the
236 South East of the ISC bulletin epicenter, and to the West of the epicenter provided in
237 the ISC-EHB bulletin. The differences in the location estimates are likely due to both
238 different weightings of the phase arrivals and differences in the location algorithms. De-
239 tails of improvements to the ISC location algorithm can be found in Bondár and Storchak
240 (2011).

241 To summarize, with the available seismic stations, there is a lateral uncertainty of
242 at least 10 km in the epicentral estimates. The epicenter from the ISC-EHB bulletin
243 appears to be an outlier and, given the set of arrivals from which this solution is formed,
244 the quoted 95% confidence interval would appear to be optimistic. We can move the
245 epicenter estimate by several km by changing the observing network alone, but never by
246 more than around 10 km. Had the seismic signals from this event had characteristics of
247 an explosion, the confidence region from the seismic signals is sufficient for the criteria
248 for a permissible On-Site-Inspection following Entry Into Force of the Comprehensive
249 Nuclear Test-Ban-Treaty. The treaty text states “The area of an on-site inspection shall
250 be continuous and its size shall not exceed 1,000 square kilometres. There shall be no
251 linear distance greater than 50 kilometres in any direction.” (UN, 1998). Even with
252 the existing network (and there are no non-IMS stations in the bulletins considered here
253 at any significantly closer distances or covering any significant azimuthal gaps), Figure

254 4 indicates that the location uncertainty is well within these limits. The completed
255 IMS, as listed in the treaty text, contains in addition stations not currently operating
256 that would likely have improved the constraints on this event (in particular, the Luxor
257 array in Egypt: $26.0^{\circ}\text{N } 33.0^{\circ}\text{E}$, not yet constructed, and the BGCA 3-component
258 station in the Central African Republic: $5.176^{\circ}\text{N}, 18.424^{\circ}\text{E}$, installed but not currently
259 operational). Another IMS 3-component station, KOWA, in Mali, is now operational but
260 was not at the time of this earthquake. (Data from IU.KOWA is openly available to the
261 community via IRIS.) There are few opportunities for further reducing the uncertainty in
262 the seismic location estimates without additional, closer, stations. For example, there are
263 no nearby seismic events from which we could perform a calibrated or relative location
264 estimate (e.g. Douglas, 1967, and subsequent studies of joint epicentral determination and
265 multiple event location). The scarcity of seismic observations in the region also means
266 that regional 3D seismic velocity models remain unrefined and uncalibrated.

267 **4 Surface displacement from the 18 January 2017** 268 **Event using InSAR Data**

269 In the case of remote continental earthquakes, with a sparsity of near-field seismological
270 data, the recently-developed global coverage of satellite radar offers an additional dataset
271 to which may help constrain earthquake locations, and complement those constraints
272 available from seismology. The limiting factor in locating an earthquake using satellite
273 geodesy is not directly the magnitude of the earthquake, but instead the amplitude of
274 the surface deformation, and whether any signal can be detected. Whilst the Ténéré
275 earthquake is lower magnitude than typically studied using InSAR (e.g., Weston et al,
276 2012; Funning and Garcia, 2019), other small-magnitude events have been detected in
277 the past (Lohman and Simons, 2005; Ritz et al, 2020), in cases where the earthquake
278 is very shallow, allowing higher-amplitude near-fault displacements to be expressed at
279 the surface. Whereas converting remote seismological observations to an source location
280 can be subject to major uncertainties on the scale of 10's of kilometres, particularly
281 relating the velocity structure, geodetic measurements offer the direct detection of near-
282 fault displacement, in the ideal case where a fault breaks the surface, can determine the
283 fault location with pixel-scale resolution (typically 10's metres). Therefore, whilst InSAR
284 offers no constraint on the earthquake origin time, places no constraints on the rupture
285 kinematics, and, for small-magnitude events, can only detect shallow sources, it can offer
286 a valuable complement to seismological observations, placing precise constraints on the
287 location of the rupture plane.

288 To supplement the available seismic data, we process interferometric synthetic aper-
289 ture radar (InSAR) images for the source region using data from the European Space

290 Agency’s Sentinel-1 satellites. We use acquisitions that span the earthquake date, and
291 construct interferograms using all potential pairs where the earthquake occurs within a
292 timespan of up to four consecutive acquisitions (Figure 5). Processing was carried out
293 using the LiCSAR system (Lazecký et al, 2020). Due to the remote location, only ascend-
294 ing track data were being routinely acquired at the time of our study earthquake, with a
295 12-day repeat time. Coherence in the region at such short temporal baselines is extremely
296 high. Given the lack of major topographic features, there is minimal topographically-
297 correlated atmospheric noise, although all interferograms are subject to long-wavelength
298 noise presumed to result from atmospheric variation (see Figures 5 and 6). One SAR
299 acquisition (20161216) features NE-SW orientated bands whose origin is uncertain, but
300 which are clearly unrelated to either the regional tectonics or our study earthquake.

301 All coseismic interferograms feature a small, roughly circular, displacement signal at
302 $\sim 19.6^\circ$ N, 10.6° E, highlighted by the black circle on Figure 5. This signal displays a spa-
303 tial pattern as expected for a small-magnitude earthquake, is at a wavelength where we
304 would expect the deformation signal from a $m_b 4.3$ to be (1 – 5 km, based on established
305 earthquake scaling relationships: Wells and Coppersmith, 1994), is common to all inter-
306 ferograms that span the earthquake date, and is not present in any interferograms that
307 do not span the earthquake (see Figure 6 for examples). We are therefore confident that
308 this signal relates to our study earthquake, despite the small amplitude of the observed
309 signal.

310 To improve the resolution of this signal, we construct a simple linear stack of 3
311 fully independent interferograms (20161204-20170202, 20161228-20170226, and 20170109-
312 20170310 from Figure 5 – stack shown in Figure 7a). To remove long-wavelength atmo-
313 spheric effects, and to isolate signals at wavelengths likely to be related to a $m_b 4.3$ earth-
314 quake, we spatially filter the InSAR data using a 4-pole Butterworth filter, bandpassed
315 between 15000 and 500 metres (Figure 7b).

316 The resulting stack shows a clear, coherent line-of-sight displacement of up to 6 mm.
317 Only one lobe of the deformation field is clearly visible, and although there are indica-
318 tions on the filtered stack of opposite-polarity displacement lobes to the northeast and
319 southeast of the main deformation lobe, these are insufficiently clear to permit the deter-
320 mination of a focal mechanism. We visually assess that the causative fault plane most
321 likely lies to the southeast or northeast of the peak in displacement. The deformation
322 pattern shows no clear discontinuities in phase, either on the stack or on individual in-
323 terferograms, suggesting that the rupture did not break the surface, and that the top
324 of the fault rupture patch is buried. That there is an observable signal at all, however,
325 from such a small-magnitude event, indicates that the earthquake must have been com-
326 paratively shallow (~ 10 km), consistent with the lack of any clearly separated depth
327 phases in the seismic data (see Figure 2). In the case of this earthquake, located in the
328 sandy Ténéré desert, we consider it likely that the earthquake ruptured to the top of

329 the consolidated bedrock, but that the deformation signal is subsequently blanketed by
330 overlying less consolidated sandstones, less able to sustain coseismic rupture.

331 5 Conclusions and Discussion

332 Figure 7 shows both seismological and geodetic constraints on the location of the 2017
333 Ténéré earthquake. Of the four catalogue locations published by seismological agencies
334 only those from the CTBT and the initial ISC catalogue are consistent with the more
335 precise location information offered by the InSAR displacement pattern. The location
336 from the NEIC lies marginally too far east, but within its own uncertainty envelope of
337 the geodetic location, whilst the ISC-EHB location lies ~ 15 km to the east-southeast
338 of the geodetic location, substantially beyond its quoted uncertainty interval from the
339 geodetically-observed displacement signal (Figure 3).

340 Comparison of geodetic and seismological location is not simple – the two approaches
341 are measuring slightly different aspects of the earthquake. Seismological locations like
342 those applied to this earthquake give a hypocentre – the point of rupture initiation. In
343 contrast, geodetic data like that used here has no capacity to constrain the earthquake
344 initiation, or its rupture process, in time, as the displacement seen in the interferograms is
345 the result of the complete earthquake rupture. In this case, we are unable to solve robustly
346 for a causative fault plane from the InSAR data, but even if we could, the earthquake
347 hypocentre could still lie anywhere on that rupture plane. For larger earthquakes, with
348 rupture lengths of $> 5km$, this can pose additional location problems. However, for
349 a small-magnitude event like the 2017 Ténéré earthquake, where the rupture length is
350 likely to be $\sim 5km$ or less, this discrepancy between the seismological hypocentre and
351 the geodetic fault rupture will be small, compared to the uncertainties in seismological
352 location.

353 Seismological locations are subject to uncertainty in the solid-Earth velocity structure
354 along the full ray path from source to receiver. In the case of the locations shown in Figure
355 3 and 4, the relative travel-time difference between all the locations shown is $< 0.5s$
356 for regional arrivals and $< 0.2s$ for teleseismic arrivals. As demonstrated in Figure 2,
357 the majority of arrivals are emergent, and picking a precise onset is usually subject to
358 uncertainties on at least this magnitude. This is then compounded by the variation in
359 predicted travel times between different velocity models. Many location routines use a
360 standard global 1-dimensional velocity structure. Inclusion of the 3D Earth structure,
361 whilst possible (e.g. Simmons et al, 2021, and references therein), remains subject to
362 relatively large uncertainties in areas like Saharan Africa, where coverage from both
363 sources and stations is very poor. In this region, the variation in predicted travel times
364 between simple 1D and more complex 3D velocity models can add an additional $0.5s$ in
365 travel time uncertainty, equating to a spatial difference on the order of 10 – 20 km. In

366 contrast, locations based on geodetic data are subject to uncertainty derived only from
367 the very-near source elastic structure. For shallow earthquakes, in particular, the impact
368 that this has on geodetic earthquake location is minimal.

369 The consideration of both InSAR and seismological data for small magnitude earth-
370 quakes, as shown here, therefore demonstrates the potential for geodetic data to both
371 supplement, and potentially calibrate, seismological earthquake location, allowed the de-
372 termination of high-precision absolute spatial locations for small earthquakes with small
373 rupture lengths. Such characterisation has several potential applications. Firstly, such
374 high precision location constraints have the potential to contribute to the monitoring and
375 discrimination capabilities of the CTBT, particularly in remote areas, far from near-field
376 seismological instrumentation. Secondly, high-precision geodetic earthquake locations
377 can be used to calibrate regional seismological locations, which are often subject to large
378 systematic uncertainties due to biases in velocity structure and in network geometry.
379 Thirdly, in cases where accurate arrival times can be determined, precise locations allow
380 the use of small earthquakes in remote places to be used for the validation of tomographic
381 models for the solid-Earth velocity structure, supplementing sparse available equivalents
382 from controlled-source seismic signals (usually explosions: Bondár and McLaughlin,
383 2009).

384 Our study on the 2017 Ténéré therefore illustrates the potential for satellite radar
385 to supplement the monitoring capabilities of traditional seismological networks for earth-
386 quake location, particularly in remote areas, and particularly in areas with high coherence.
387 As the footprint of satellite missions, and the coverage of routine processing, expands,
388 the potential for InSAR to be brought in to routine earthquake monitoring will only
389 increase. Seismic detectability maps have long been employed to estimate thresholds for
390 the magnitudes of seismic disturbances which can confidently be detected and location in
391 a given region for a given monitoring network (e.g. Kväerna and Ringdal, 2013). Going
392 forwards, we would recommend the development of global detectability maps for geode-
393 tic observation, although we recognise that these would need to build in the limitations
394 posed by the tradeoff between depth and magnitude of displacement detectability, and
395 time-variable nature of both decorrelation and non-tectonic noise in satellite radar.

396 The 2017 Ténéré earthquake also illustrates the role that data not routinely available
397 to the academic community play in earthquake location. For both the USGS and the ISC
398 sets of arrivals used in our relocation (see Figure 4), restricting the arrivals used to only
399 Open Access data leads to a marked increase the location uncertainty. Whilst the InSAR
400 data used here, from the European Space Agency’s Sentinel-1 mission, is freely available,
401 the same is not necessarily true for all radar missions. Whilst the radar coherence in the
402 Ténéré is extremely good, allowing up to resolve such small displacements, conducting
403 such work elsewhere, particularly in more vegetated environments, will likely benefit from
404 the use of a range of satellites with different mission parameters, particularly wavelength,

405 and may lead to a similar disparity between Open Access and restricted data that we see
406 in the seismological datasets.

407 **Acknowledgements**

408 All published location estimates were obtained from the bulletin of the International Seis-
409 mological Center (ISC, 2021) http://www.isc.ac.uk/cgi-bin/web-db-v4?event_id=619603285
410 (ISC, last accessed November 2021). The USGS/NEIC solution with phase arrival times
411 are published on <https://earthquake.usgs.gov/earthquakes/eventpage/us10007u0v/executive>
412 (United States Geological Survey, last accessed November 2021). The bayesloc program
413 is obtained from

414 <https://www-gs.llnl.gov/nuclear-threat-reduction/nuclear-explosion-monitoring/bayesloc>

415 TJC was supported in this work by the Royal Society under URF\R1\180088. TJC was also
416 supported through COMET, the UK Natural Environment Research Council’s Centre for the
417 Observation and Modelling of Earthquakes, Volcanoes, and Tectonics. We thank Milan Lazecky
418 for his assistance with processing the InSAR data, and Tim Wright for useful discussions.

419 All maps in this paper are created using GMT software (Wessel et al, 2019). Seismograms
420 in Figure 1 and 2 were plotted using Obspy (Beyreuther et al, 2010).

421 **References**

422 Beyreuther M, Barsch R, Krischer L, Megies T, Behr Y, Wassermann J (2010) ObsPy:
423 A Python Toolbox for Seismology. *Seismological Research Letters* 81:530–533, DOI
424 10.1785/gssrl.81.3.530

425 Blandford R (1974) An automatic event detector at the Tonto Forest Seismic Observa-
426 tory. *Geophysics* 39(5):633–643, DOI 10.1190/1.1440453, URL [http://dx.doi.org/
427 10.1190/1.1440453](http://dx.doi.org/10.1190/1.1440453)

428 Bondár I, McLaughlin K (2009) A New Ground Truth Data Set For Seismic Studies.
429 *Seismological Research Letters* 80, DOI 10.1785/gssrl.80.3.465

430 Bondár I, Storchak D (2011) Improved location procedures at the International Seismolog-
431 ical Centre. *Geophysical Journal International* 186(3):1220–1244, DOI 10.1111/j.1365-
432 246x.2011.05107.x, URL <http://dx.doi.org/10.1111/j.1365-246x.2011.05107.x>

433 Bondár I, Myers SC, Engdahl ER, Bergman EA (2004) Epicentre accuracy based on
434 seismic network criteria. *Geophysical Journal International* 156(3):483–496, DOI
435 10.1111/j.1365-246x.2004.02070.x, URL [http://dx.doi.org/10.1111/j.1365-246x.
436 2004.02070.x](http://dx.doi.org/10.1111/j.1365-246x.2004.02070.x)

437 Davies D, Kelly DJ, Filson JR (1971) The VESPA process for the analysis of seismic
438 signals. *Nature* 232:8–13

439 Douglas A (1967) Joint Epicentre Determination. *Nature* 215(5096):47–48, DOI 10.1038/
440 215047a0, URL <http://dx.doi.org/10.1038/215047a0>

441 Funning G, Garcia A (2019) A systematic study of earthquake detectability using
442 Sentinel-1 Interferometric Wide-Swath data. *Geophysical Journal International* 216,
443 DOI 10.1093/gji/ggy426

444 Gibbons SJ, Antonovskaya G, Asming V, Konechnaya YV, Kremenetskaya E, Kværna
445 T, Schweitzer J, Vaganova NV (2016) The 11 October 2010 Novaya Zemlya Earth-
446 quake: Implications for Velocity Models and Regional Event Location. *Bulletin of the*
447 *Seismological Society of America* 106(4):1470–1481, DOI 10.1785/0120150302, URL
448 <http://dx.doi.org/10.1785/0120150302>

449 ISC (2021) International Seismological Centre on-line Bulletin. [https://doi.org/10.](https://doi.org/10.31905/D808B830)
450 [31905/D808B830](https://doi.org/10.31905/D808B830), DOI 10.31905/D808B830

451 ISC-EHB (2021) International Seismological Centre ISC-EHB dataset. [https://doi.](https://doi.org/10.31905/PY08W6S3)
452 [org/10.31905/PY08W6S3](https://doi.org/10.31905/PY08W6S3), DOI 10.31905/PY08W6S3

453 ISC-GEM (2021) International Seismological Centre ISC GEM earthquake catalog.
454 <https://doi.org/10.31905/d808b825>, DOI 10.31905/d808b825

455 Kværna T, Ringdal F (2013) Detection Capability of the Seismic Network of the Inter-
456 national Monitoring System for the Comprehensive Nuclear Test-Ban-Treaty. *Bulletin*
457 *of the Seismological Society of America* 103(2A):759–772, DOI 10.1785/0120120248,
458 URL <http://dx.doi.org/10.1785/0120120248>

459 Lazecký M, Spaans K, González P, Maghsoudi Y, Morishita Y, Albino F, Elliott J,
460 Greenall N, Hatton E, Hooper A, Juncu D, McDougall A, Walters RJ, Watsom C,
461 Weiss J, Wright T (2020) LiCSAR: an Automatic InSAR Tool for Measuring and Mon-
462 itoring Tectonic and Volcanic Activity. *Remote Sensing* 12, DOI 10.3390/rs12152430

463 Lohman R, Simons M (2005) Locations of selection small earthquakes in the Zagros
464 mountains. *Geochemistry, Geophysics, Geosystems* 6, DOI 10.1029/2004GC000849

465 Myers SC, Johannesson G, Hanley W (2007) A Bayesian hierarchical method for
466 multiple-event seismic location. *Geophysical Journal International* 171(3):1049–1063,
467 DOI 10.1111/j.1365-246x.2007.03555.x, URL [http://dx.doi.org/10.1111/j.1365-](http://dx.doi.org/10.1111/j.1365-246x.2007.03555.x)
468 [246x.2007.03555.x](http://dx.doi.org/10.1111/j.1365-246x.2007.03555.x)

- 469 Myers SC, Simmons NA, Johannesson G, Matzel E (2015) Improved Regional and
470 Teleseismic P-Wave Travel-Time Prediction and Event Location Using a Global
471 3D Velocity Model. *Bulletin of the Seismological Society of America* 105(3):1642–
472 1660, DOI 10.1785/0120140272, URL [https://pubs.geoscienceworld.org/bssa/
473 article/105/3/1642-1660/332170](https://pubs.geoscienceworld.org/bssa/article/105/3/1642-1660/332170)
- 474 Ritz J, Baize S, Ferry M, Larroque C, Audin L, Delouis B, Mathot E (2020) Surface
475 rupture and shallow fault reactivation during the 2019 MW 4.9 Le Teil earthquake,
476 France. *Communications Earth and Environment* 1, DOI 10.1038/s43247-020-0012-z
- 477 Rost S, Thomas C (2009) Improving Seismic Resolution Through Array Processing
478 Techniques. *Surveys in Geophysics* 30:271–299, URL [http://dx.doi.org/10.1007/
479 s10712-009-9070-6](http://dx.doi.org/10.1007/s10712-009-9070-6), doi:10.1007/s10712-009-9070-6
- 480 Simmons NA, Myers SC, Morency C, Chiang A, Knapp DR (2021) SPiRaL: a multiresolu-
481 tion global tomography model of seismic wave speeds and radial anisotropy variations in
482 the crust and mantle. *Geophysical Journal International* 227:1366–1391, DOI 10.1093/
483 gji/ggab277, URL <https://academic.oup.com/gji/article/227/2/1366/6324570>
- 484 UN (1998) CTBT, Comprehensive Nuclear Test-Ban-Treaty. United Nations, Dept. for
485 Disarmament Affairs and Dept. of Public Information, New York. [https://www.
486 ctbto.org/the-treaty/treaty-text/](https://www.ctbto.org/the-treaty/treaty-text/)
- 487 Wells D, Coppersmith K (1994) New Empirical Relationships among Magnitude, Rupture
488 Length, Rupture Width, Rupture Area, and Surface Displacement. *Bulletin of the
489 Seismological Society of America* 84:974–2001
- 490 Wessel P, Luis JF, Uieda L, Scharroo R, Wobbe F, Smith WHF, Tian D (2019) The
491 Generic Mapping Tools Version 6. *Geochemistry, Geophysics, Geosystems* 20(11):5556–
492 5564, DOI 10.1029/2019GC008515
- 493 Weston J, Ferreira A, Funning G (2012) Systematic comparisons of earthquake source
494 models determined using InSAR and seismic data. *Tectonophysics* 532-535, DOI 10.
495 1016/j.tecto.2012.02.001

Catalogue	Origin time (UTC)	Latitude (°)	Longitude (°)	Depth (km)	m_b
IDC	2017/01/18 21:48:19.39	19.5947	10.6106	0.0 ^{<i>f</i>}	4.2
ISC	2017/01/18 21:48:21.08	19.5847	10.6018	10.0 ^{<i>f</i>}	4.3
NEIC	2017/01/18 21:48:22.14	19.6049	10.6491	10.0 ^{<i>f</i>}	4.6
ISC-EHB	2017/01/18 21:48:21.08	19.5847	10.6018	10.0 ^{<i>f</i>}	–

Table 1: Routine catalogue locations for the 2017 Ténéré earthquake. ^{*f*}Depths were fixed *a priori* during location determination.

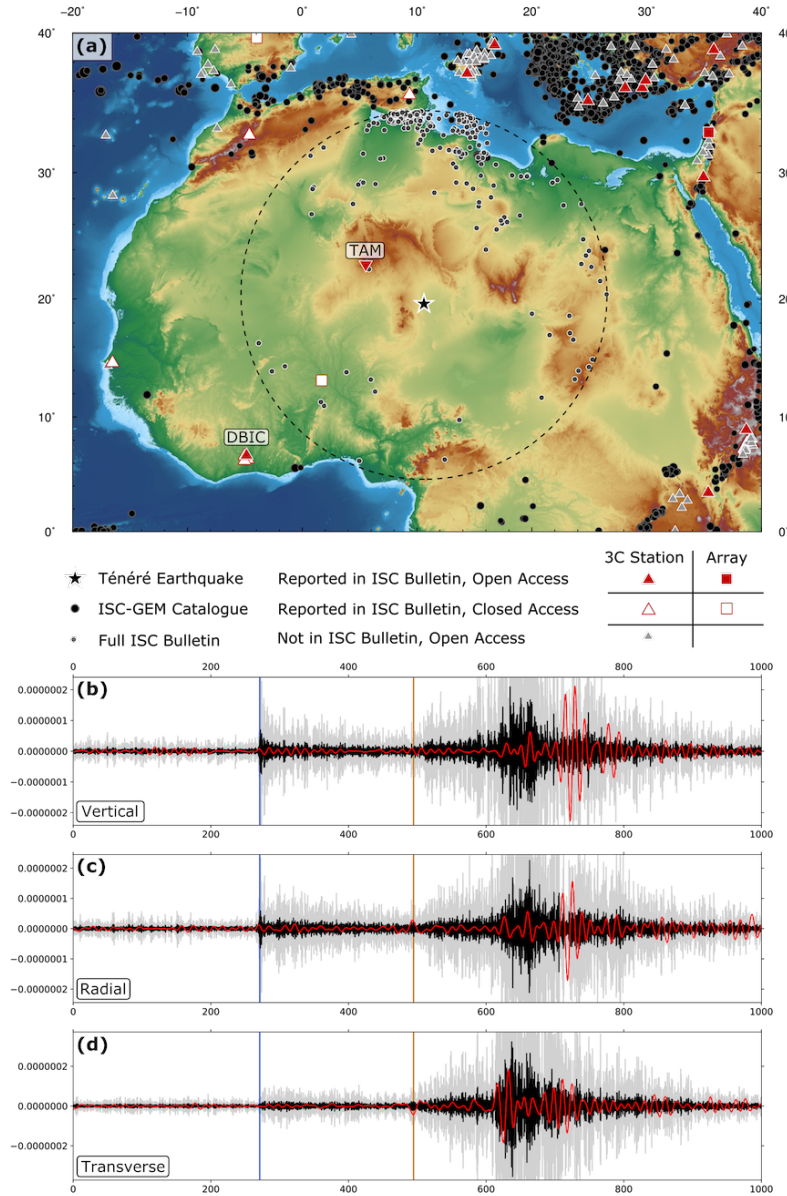


Figure 1: (a) Regional map, showing the 2017 Ténéré earthquake and distribution of observing seismometers. Red filled symbols indicate stations reported in the ISC Bulletin that are Open Access, White-filled symbols are those reported in the ISC Bulletin that are closed, grey are those Open Access 3-component stations not reported in the ISC Bulletin. Inverted red triangle shows the location of the seismometer at Tamanrasset (Algeria), usually reporting to the ISC Bulletin, but inoperative at the time of the 2017 Ténéré earthquake. Black circles show all earthquakes in the ISC-GEM catalogue. Grey circles show every earthquake recorded in the full ISC Bulletin within 15° of the 2017 Ténéré earthquake. (b) Vertical component waveform from DBIC (location shown in (a)). Black trace is filtered between 1.0 and 4.0 Hz, red between 0.02 and 0.08 Hz, to isolate surface wave arrivals, grey is the same as black, with the amplitude scaled by a factor of 5 to emphasise the body wave arrivals. Blue and green bars show the predicted P and S arrival times. (c) as in (b), but showing the radial component waveform. (d) as in (b), but showing the transverse component waveform.

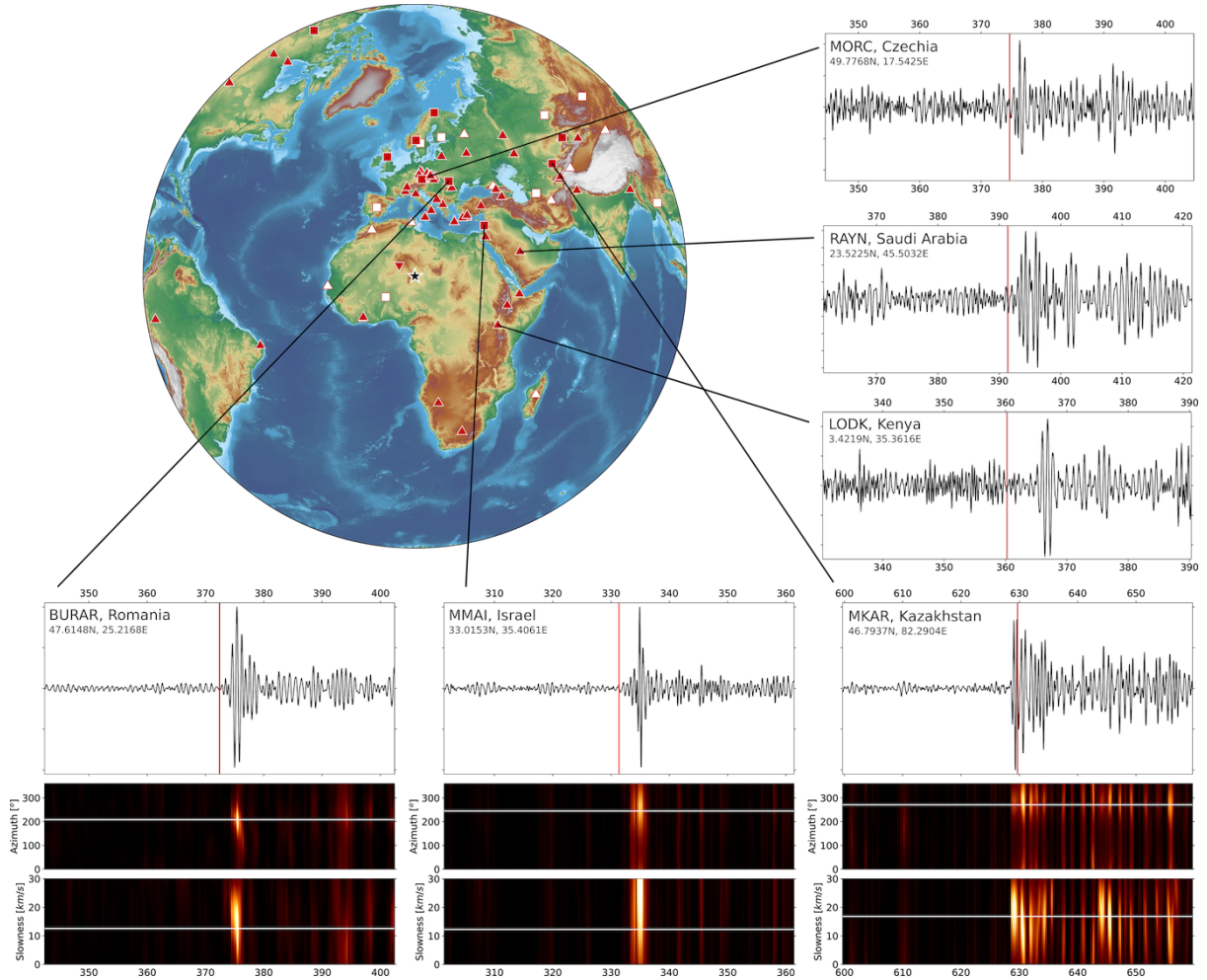


Figure 2: Global station distribution (symbols as in Figure 1). Left panels show 3 vertical component waveforms, filtered between 1 – 3 Hz, from 3-component instruments RAYN, MORC, and LODK. Vertical red line shows the predicted P -wave arrival, based on the NEIC location. Lower panels show data from three small-aperture seismic arrays (Bucovina, Mount Meron, and Makanchi), again filtered between 1 – 3 Hz. Top panel shows the beamformed waveform, based on the NEIC location. Lower panels show sweeps through slowness and azimuth space (c.f. Davies et al, 1971), with colour indicating array coherence using the F -statistic (e.g. Blandford, 1974). White lines show the predicted slowness and azimuth for P -wave arrivals from the Ténéré earthquake.

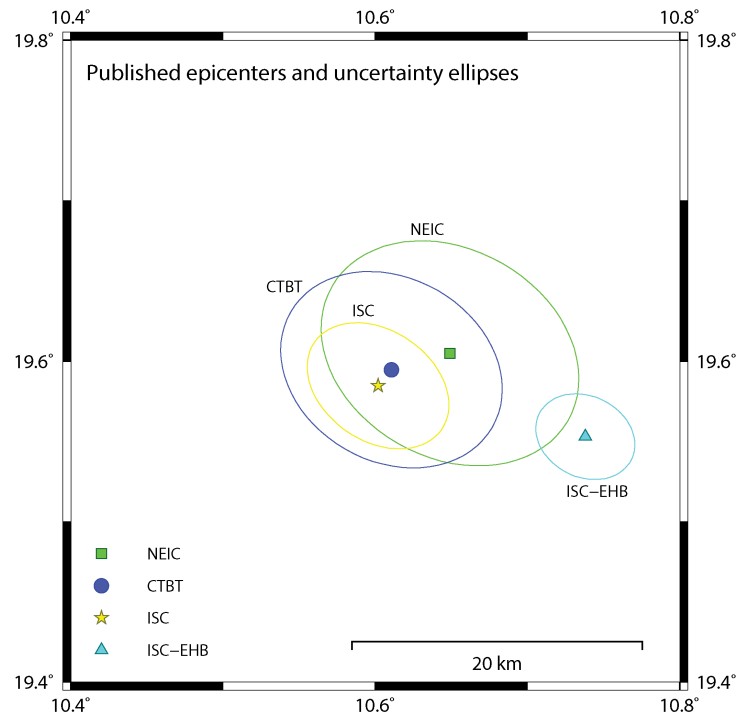


Figure 3: Published location estimates and corresponding 95% confidence ellipses for the January 18, 2017, Niger Earthquake. The epicenters are as provided in Table 1 and the 95% confidence ellipses have ($S_{maj}/S_{min}/Azimuth$) parameters ($18.7/14.4/125^\circ$) NEIC, ($16.0/12.7/120^\circ$) CTBT, ($10.6/7.6/125^\circ$) ISC, and ($7.1/5.6/117^\circ$) ISC-EHB with S_{maj} and S_{min} given in km.

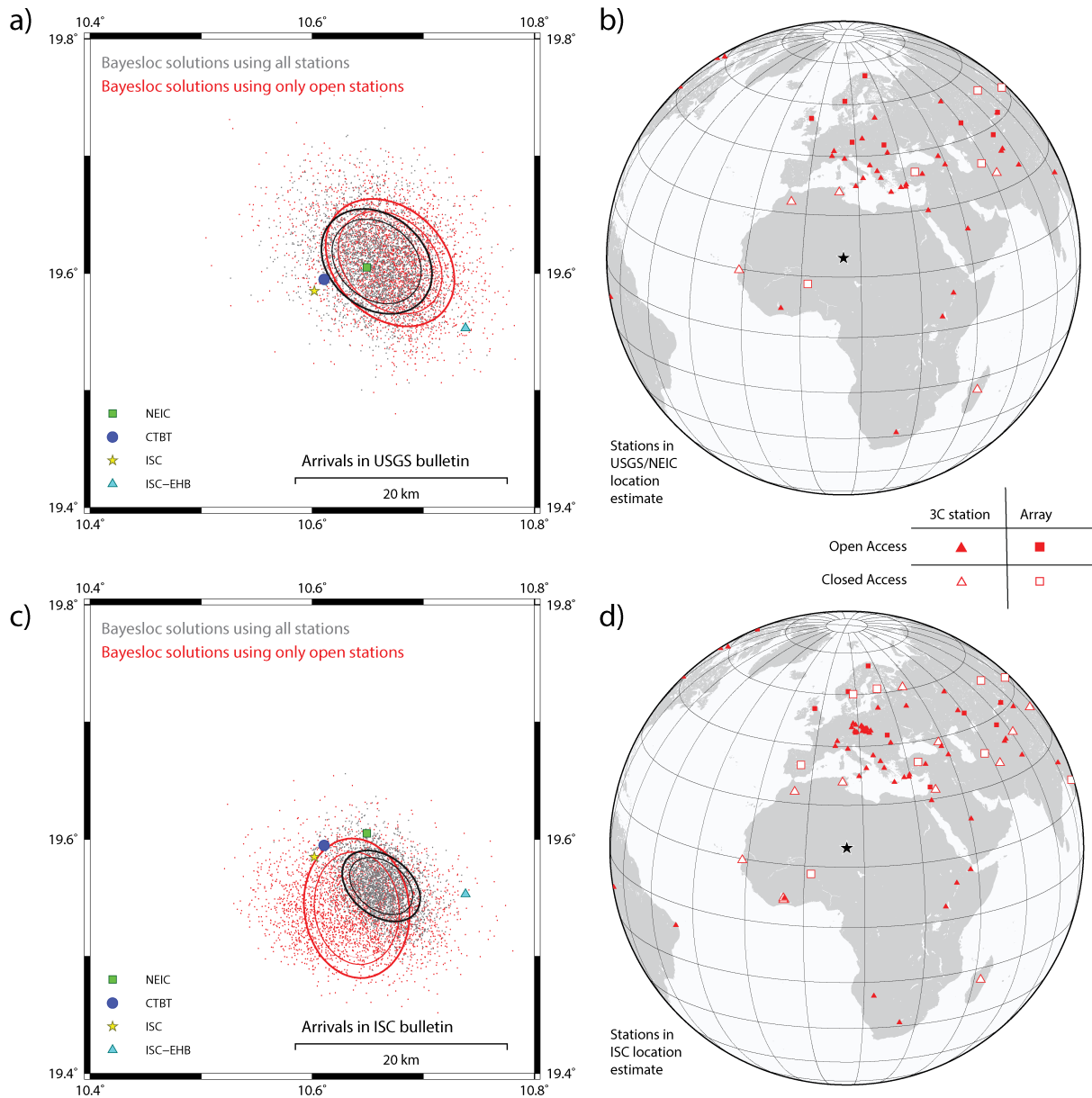


Figure 4: Location estimates obtained using the Bayesloc program with station selections as indicated. Panels (a) and (c) display clouds of the epicenters in the Bayesloc Monte Carlo Markov Chains together with the 90, 95, and 99% confidence ellipses calculated for the scatter plots. Each cloud contains 36000 points. Panels (b) and (d) display the stations used to obtain the solutions displayed in panels (a) and (c) respectively.

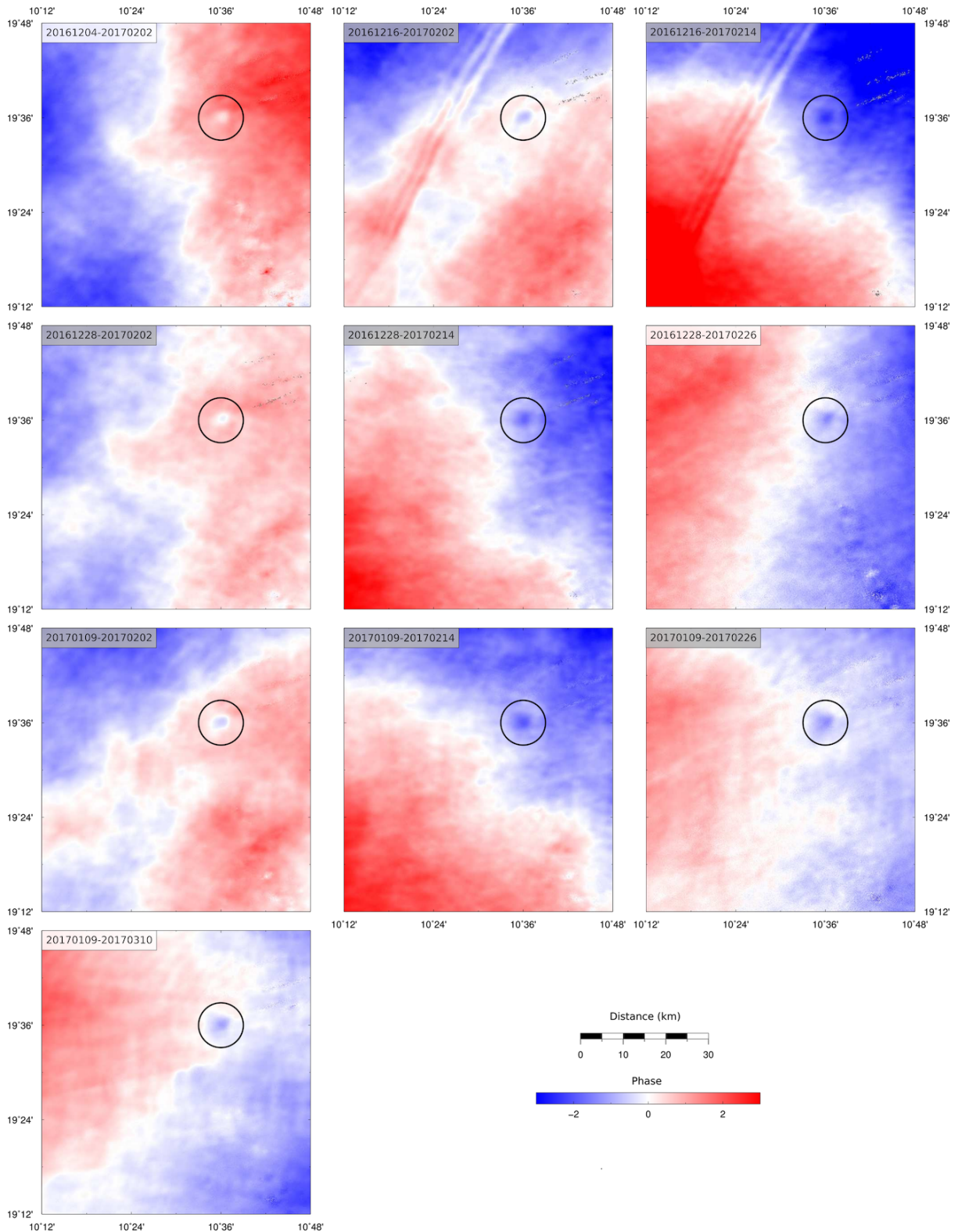


Figure 5: 10 coseismic interferograms, unwrapped. Colour scale shows multiples of the complete phase cycle. Numeric codes in the top left of each panel indicate the SAR acquisitions used to produce each interferogram. Shading behind numeric codes indicates those independent pairs used in the stack shown in Figure XX. Black circle highlights the consistent signal identified as results from the earthquake.

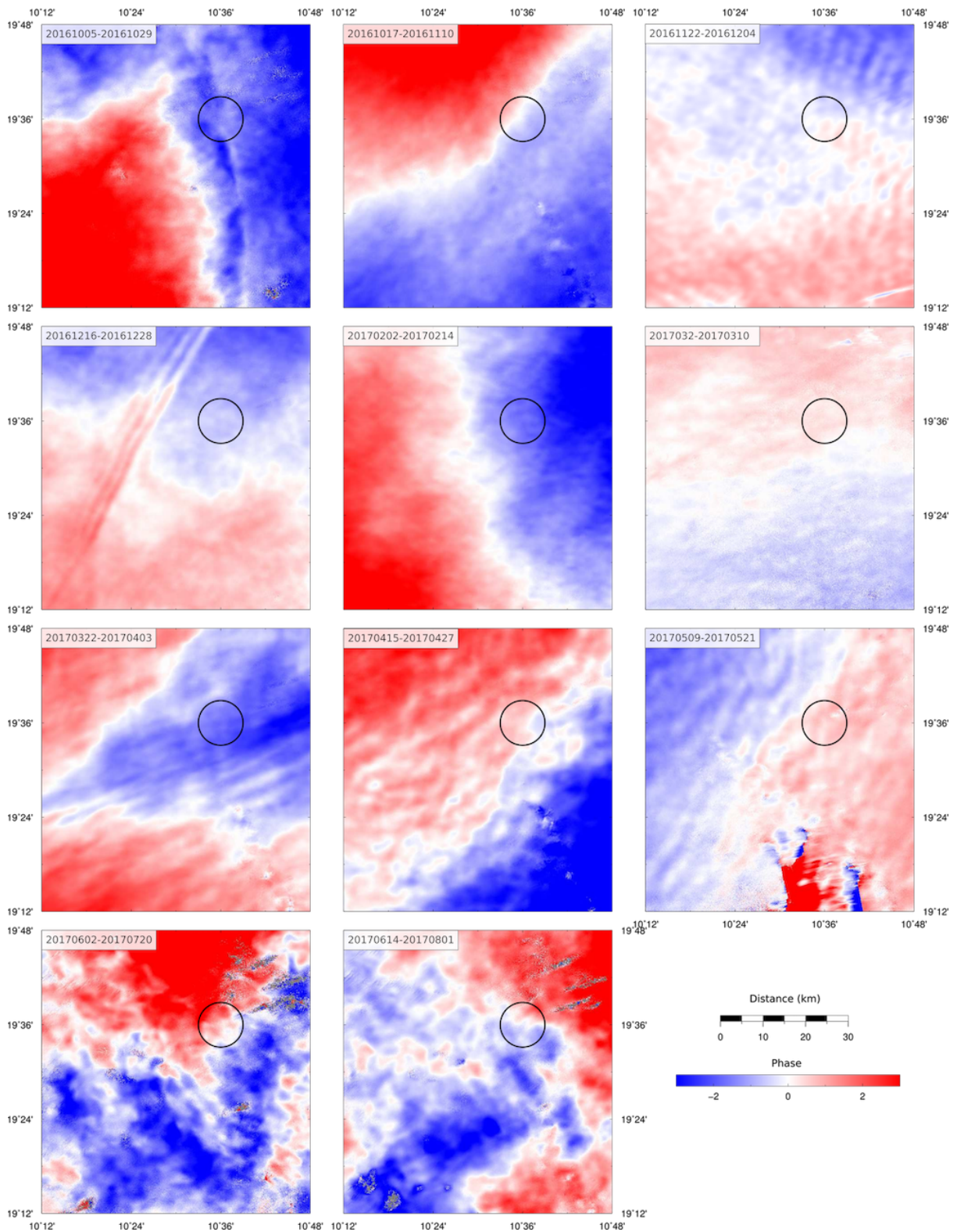


Figure 6: 11 interferograms, unwrapped, that do not span the date of the Ténéré earthquake. Numeric codes in the top left of each panel indicate the SAR acquisitions used to produce each interferogram. Black circle highlights area in which the coseismic interferograms shown in Figure 5 show a consistent deformation signal.

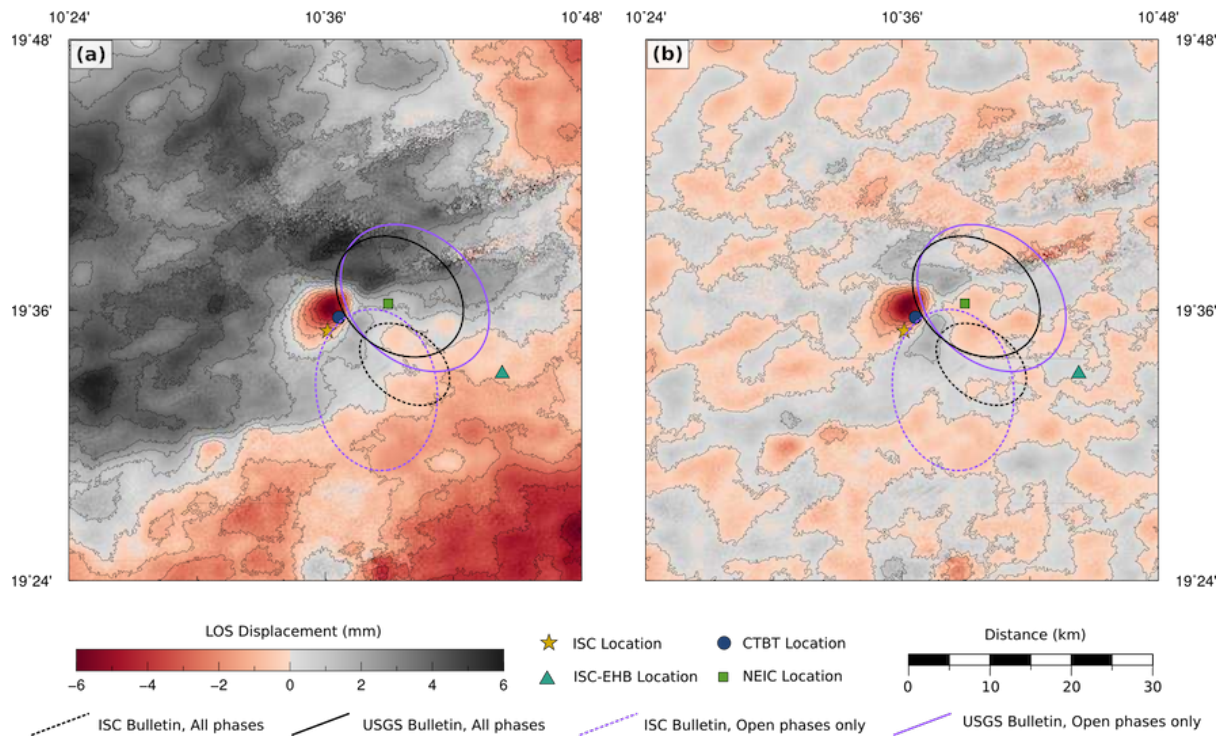


Figure 7: (a) Stacked unwrapped interferogram. (b) Stacked interferogram, filtered between 15 km and 500 m. Colour scale shows line-of-sight displacement. Symbols show seismological locations, as in Figure 3. Contours show 95% interval ellipses determined using different seismic arrival subsets, as described in Figure 4.